THE JOURNAL OF PHYSICAL CHEMISTRY A

pubs.acs.org/JPCA Article

Chemical Shift Tensors of Cimetidine Form A Modeled with Density Functional Theory Calculations: Implications for NMR Crystallography

Sean T. Holmes, Olivia G. Engl, Matthew N. Srnec, Jeffry D. Madura, Rosalynn Quiñones, James K. Harper, Robert W. Schurko,* and Robbie J. Iuliucci*

Cite This: J. Phys. Chem. A 2020, 124, 3109–3119 Read Online

ACCESS | Metrics & More | Article Recommendations | Supporting Information

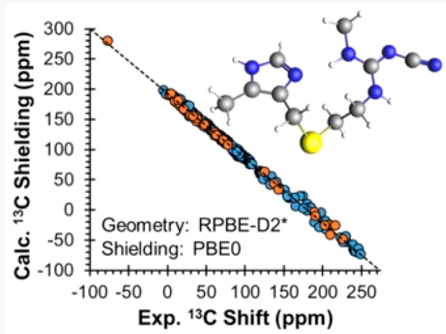

ABSTRACT: The principal components of the ^{13}C chemical shift tensors for the ten crystallographically distinct carbon atoms of the active pharmaceutical ingredient cimetidine Form A have been measured using the FIREMAT technique. Density functional theory (DFT) calculations of ^{13}C and ^{15}N magnetic shielding tensors are used to assign the ^{13}C and ^{15}N peaks. DFT calculations were performed on cimetidine and a training set of organic crystals using both plane-wave and cluster-based approaches. The former set of calculations allowed several structural refinement strategies to be employed, including calculations utilizing a dispersion-corrected force field that was parametrized using ^{13}C and ^{15}N magnetic shielding tensors. The latter set of calculations featured the use of resource-intensive hybrid-DFT methods for the calculation of magnetic shielding tensors. Calculations on structures refined using the new force-field correction result in improved values of ^{15}N magnetic shielding tensors (as gauged by agreement with experimental chemical shift tensors), although little improvement is seen in the prediction of ^{13}C shielding tensors. Calculations of ^{13}C and ^{15}N magnetic shielding tensors using hybrid functionals show better agreement with experimental values in comparison to those using GGA functionals, independent of the method of structural refinement; the shielding of carbon atoms bonded to nitrogen are especially improved using hybrid DFT methods.

■ INTRODUCTION

The assignment of distinct peaks to unique atomic sites is a fundamental step in the analysis of solid-state NMR (SSNMR) data. This is particularly challenging for ^{13}C and ^{15}N NMR spectra of moderate to large molecular systems, because chemically and magnetically distinct nuclei in similar environments often give rise to peaks with similar or identical chemical shift values. In such cases, one-dimensional NMR techniques that rely solely upon the measurement of isotropic chemical shifts can lead to incorrect peak assignments, even when conducted with a variety of double-resonance conditions aimed at site differentiation.[1] Multidimensional NMR techniques can often resolve these ambiguities; however, measurements of the principal components of the chemical shift tensors provide a robust alternative for making assignments and also offer a data set rich in information on electronic structure and local symmetries that can be used for structural interpretation and enhanced NMR crystallographic modeling.[2−10]

Computational modeling of anisotropic NMR interactions (*i.e.*, magnetic shielding, scalar coupling, and electric-field gradient (EFG) tensors) using density functional theory (DFT) provides a method of relating NMR parameters to electronic structure.[11−15] For the calculation of ^{13}C and ^{15}N magnetic shielding tensors in crystals, one can employ either periodic or cluster-based structural models to account for long-range lattice effects.[16−23] The combination of the two allows one to explore the effects of various types of structural refinements or DFT approximations that affect the accuracy of calculated ^{13}C and ^{15}N magnetic shielding tensors in comparison to their experimentally measured counterparts. These considerations are of vital importance for making peak assignments for solids with known crystal structures, or to validate proposed structures using an NMR crystallography approach.

Because of the relationship between computed NMR parameters and molecular-level structure, refinement of crystal structures determined from diffraction methods is a prerequisite for accurate calculations of NMR parameters.[24−27] In particular, the positions of hydrogen atoms are generally determined inaccurately from X-ray diffraction (XRD) techniques and must be refined before SSNMR parameters can be calculated for these

Received: January 15, 2020
Revised: March 31, 2020
Published: April 1, 2020

structures.[6,7,28−32] Recently, it has been shown that semi-empirical force-field corrections that account for the effects of dispersion[33−35] in plane-wave DFT calculations are essential for refining crystal structures to the degree necessary for the accurate prediction of certain NMR parameters, including EFG tensors.[28,29,36] Computationally derived SSNMR parameters can be used to design new force fields to assist in the enhanced refinement of crystal structures and to obtain increasingly accurate theoretical EFG and magnetic shielding tensor parameters that are otherwise unavailable from methods that do not incorporate these techniques.

Calculations of ^{13}C and ^{15}N magnetic shielding tensors using GGA functionals (as is typical for calculations employing the periodic GIPAW formalism) often result in inferior agreement with experiment compared to calculations using hybrid functionals.[16−20] Because the introduction of an admixture of Hartree−Fock exchange (HFX) results in computations that are generally too protracted to implement within the plane-wave formalism, cluster- or fragment-based modeling of the extended lattice is often necessary to account for long-range contributions to the shielding tensors.[37] Thus, the combination of plane-wave DFT calculations for structural refinement and cluster-based models for implementing an admixture of HFX could improve substantially the prediction of magnetic shielding tensors in organic crystals.

This study focuses on the active pharmaceutical ingredient (API) cimetidine (Scheme 1), a histamine H_2-receptor antagonist that was one of the first APIs developed by rational drug design[38] and which has been the subject of many SSNMR studies.[7,39−47] Cimetidine crystallizes in many forms, including four anhydrous polymorphs (A−D), a monohydrate, and several hydrochloride salts; of these, Form A ($P2_1/c$, $Z' = 1$, $Z = 4$) is commonly present in dosage forms of the drug.[48] Most of the known forms of cimetidine have been characterized by ^{1}H−^{13}C CP/MAS NMR, which is useful for rapid fingerprinting and phase identification (including the detection of impurity phases).[39−41] The crystal structures of several forms of cimetidine have been solved using NMR crystallographic techniques. Middleton and co-workers redetermined the crystal structure of cimetidine Form A using powder XRD (PXRD) and conformational constraints introduced by ^{15}N−^{13}C and ^{13}C−^{13}C REDOR spectroscopy.[42−44] ^{1}H−^{13}C CP/MAS NMR data and DFT calculations played a key role in determining the crystal structure of cimetidine HCl from analysis of PXRD data.[40] Nishiyama and co-workers used a combination of electron diffraction, DFT calculations, and multinuclear SSNMR to determine the structure of cimetidine Form B.[49] Kalakewich et al. measured the ^{15}N chemical shift tensors for cimetidine Form A and demonstrated that these values can be used to refine the atomic positions within the crystal structure beyond the capability of XRD.[7]

Scheme 1. Molecular Structure and Atomic Labeling Scheme of Cimetidine[a]

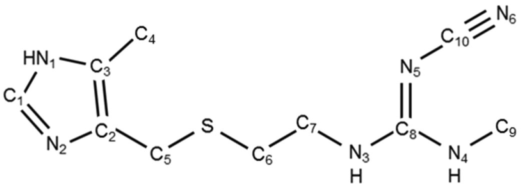

[a]Certain hydrogen atoms have been omitted for clarity.

Herein, we use experimental ^{13}C chemical shift anisotropy (CSA) measurements and calculations of carbon magnetic shielding tensors using DFT methods to provide the ten peak assignments in the ^{13}C SSNMR spectrum of cimetidine Form A. The ^{13}C SSNMR spectrum of cimetidine Form A suffers from the common pitfalls associated with spectral peak assignments, including overlapping isotropic peaks and substantial differences between the isotropic chemical shifts of the API in the solid state and aqueous solution. Several considerations for performing DFT calculations on organic solids are evaluated, including (i) geometry optimization of structures determined initially from single-crystal XRD (SCXRD) as a prerequisite for accurate prediction of magnetic shielding tensors and (ii) the use of computationally expensive hybrid DFT approaches to achieve superior agreement with experimental values of ^{13}C and ^{15}N chemical shift tensors (the former are reported herein, the latter are from work by Kalakewich et al.[7]). The insights afforded through the calculations on cimetidine (both ^{13}C and ^{15}N magnetic shielding tensors) are supported by additional calculations on a training set of organic crystals.

■ EXPERIMENTAL AND COMPUTATIONAL DETAILS

Sample Preparation. Commercial samples of cimetidine were purchased from Sigma-Aldrich. Form A of cimetidine was obtained by slow evaporation from acetonitrile.[48] The identity of the sample as Form A was confirmed *via* comparison with the ^{13}C SSNMR spectrum provided by Middleton et al.[39]

Solid-State NMR Spectroscopy. SSNMR experiments were conducted in two separate laboratories using different spectrometers and hardware. Spectra acquired at the University of Utah (Salt Lake City, Utah) used a Chemagnetics CMX console, a 14.1 T wide bore Oxford magnet [$\nu_0(^1\text{H}) = 600.18$, $\nu_0(^{13}\text{C}) = 150.93$ MHz], and a 5 mm Varian T3 HX probe. Spectra acquired at Washington and Jefferson College (Washington, Pennsylvania) used a Varian INOVA console, a 9.4 T wide bore Oxford magnet [$\nu_0(^1\text{H}) = 399.81$, $\nu_0(^{13}\text{C}) = 100.54$ MHz], and a 4 mm Varian T3 HX probe. All samples were packed into pencil-style zirconia rotors. The ^{13}C chemical shift values in all spectra were referenced externally to the methyl resonance in 3-methylglutaric acid at 18.84 ppm relative to TMS at $\delta_{iso} = 0.00$ ppm.

Routine experiments performed at 9.4 T include a ^{13}C-detected ^{1}H T_1 measurement, dipolar dephasing ^{13}C spectra, and a one-dimensional high-resolution ^{13}C spectrum. These measurements made use of ^{1}H−^{13}C CP/MAS, including a 3.0 ms Hartman−Hahn match at a 66 kHz rf field with a tangent ramp, and a sample spinning rate of $\nu_{rot} = 10.0$ kHz. In each measurement, 125 kHz ^{1}H decoupling was applied with the TPPM scheme[50] using a 4.0 μs ^{1}H π pulse and a 9° phase modulation. The recycle delay of 23 s was set on the basis of the ^{1}H T_1 of cimetidine form A determined by a ^{13}C-detected ^{1}H inversion-recovery experiment. For the ^{1}H dipolar-dephasing experiments, the dephasing delay was arrayed from 0 to 120 ms and each dephased spectrum was signal averaged for 1.5 h.

The high-resolution and five-π replicated magic angle turning (FIREMAT)[51] ^{13}C NMR spectra were acquired at 14.1 T under ^{1}H−^{13}C CP/MAS conditions at sample spinning rates of ν_{rot} = 10.5 and 1.777 kHz, respectively. The CP conditions include a Hartman−Hahn match at 71 kHz and a 7.5 ms contact time. The ^{13}C FIREMAT π pulse width was 6.5 μs. The spectra were

https://dx.doi.org/10.1021/acs.jpca.0c00421
J. Phys. Chem. A 2020, 124, 3109−3119

Scheme 2. Two Example Clusters, Pyrrole (Left) and Sulfamic Acid (Right), Including an Illustration of the Partitioning of the Basis Set between TZ2P (Ball-and-Stick Representation) and DZ Regions (Wireframe Representation)

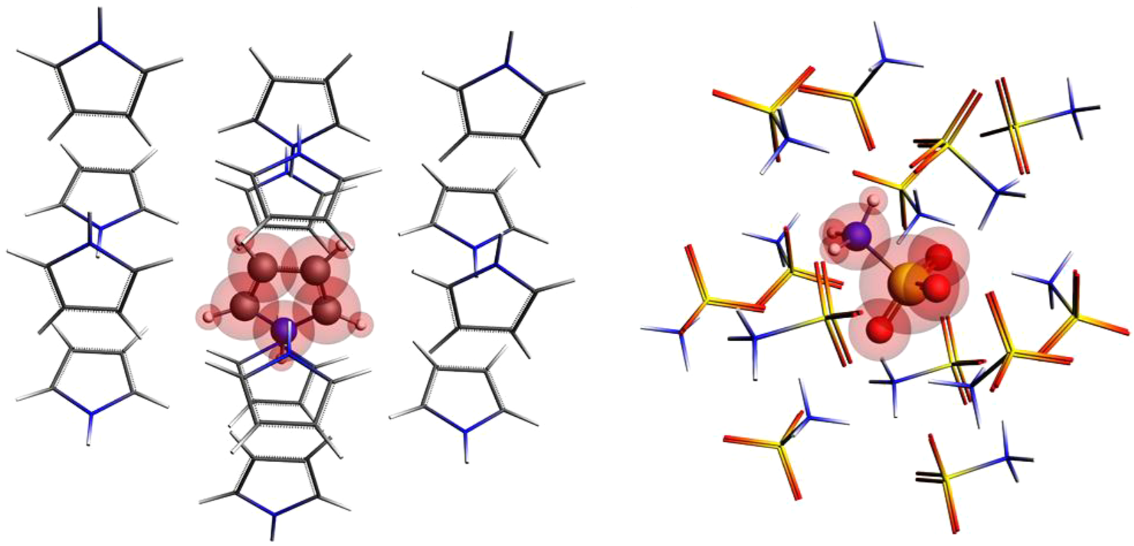

Table 1. Experimental and Calculated Principal Components of the ^{13}C Chemical Shift Tensors of Cimetidine Form A[a,b]

carbon no.		δ_{iso} (ppm)	Ω (ppm)	κ	δ_{11} (ppm)	δ_{22} (ppm)	δ_{33} (ppm)	carbon type[c]
1	exp	134.8	146.5	0.04	207.0	136.9	60.5	CH
	calc	133.6	142.5	0.11	202.2	138.8	59.7	
2	exp	135.8	139.6	0.15	202.1	142.8	62.5	quat
	calc	138.4	139.4	0.21	203.2	148.2	63.9	
3	exp	120.7	141.0	0.09	189.0	124.9	48.0	quat
	calc	118.1	132.6	0.06	183.1	120.6	50.5	
4	exp	10.5	19.0	−0.25	20.8	8.9	1.8	CH_3
	calc	12.7	23.1	−0.10	24.6	12.0	1.5	
5	exp	23.2	24.7	−0.30	36.8	20.7	12.1	CH_2
	calc	27.1	27.7	−0.35	42.6	23.9	14.8	
6	exp	28.4	36.5	0.06	46.0	28.9	9.5	CH_2
	calc	31.5	39.1	0.12	50.2	33.1	11.1	
7	exp	40.8	58.3	−0.17	71.6	37.6	13.3	CH_2
	calc	39.8	61.2	−0.09	71.3	37.9	10.2	
8	exp	161.1	138.3	0.62	215.9	189.8	77.6	quat
	calc	156.7	124.1	0.77	202.9	188.4	78.8	
9	exp	27.9	43.3	−0.17	47.2	32.4	3.9	CH_3
	calc	27.9	47.6	−0.10	48.1	35.1	0.5	
10	exp	119.2	302.4	0.62	225.3	209.3	−77.1	quat
	calc	120.3	306.5	0.77	224.7	218.1	−81.8	

[a]Calculations were performed on a structure refined at the RPBE-D2* level. The magnetic shielding tensors were calculated at the PBE0/TZ2P level. [b]The principal components of the chemical shift tensors are ranked using the frequency-ordered convention such that $\delta_{11} \geq \delta_{22} \geq \delta_{33}$. The isotropic chemical shift, span, and skew are given by $\delta_{iso} = (\delta_{11} + \delta_{22} + \delta_{33})/3$, $\Omega = \delta_{11} - \delta_{33}$, and $\kappa = 3(\delta_{22} - \delta_{iso})/\Omega$, respectively. The average error in the individual experimental principal components is estimated to be ±0.7 ppm. [c]The carbon type was established using dipolar dephasing experiments. See Figure S1 for details.

acquired with 55 kHz ^{1}H TPPM decoupling using a 9.1 ms π pulse and a phase modulation of 14° between consecutive pulses. For FIREMAT experiments, spectral widths of 26.5 and 50.5 kHz were used in the evolution and acquisition dimensions, respectively. A total of 14 evolution increments of 672 scans each were collected using a 14 s recycle delay for a total experiment time of 4.4 days. The FIREMAT data processing followed the TIGER approach.[52]

Geometry Optimizations. All geometry optimizations were performed within the CASTEP module of Biovia Materials Studio 2018.[53] Calculations were conducted on model systems based on previously determined SCXRD structures (Table S1, Supporting Information). The calculations employed the RPBE functional,[54] a plane-wave cutoff energy of 570 eV, and ZORA scalar pseudopotentials generated on the fly.[55,56] Integrals over the Brillouin zone were sampled using a Monkhorst−Pack grid with a *k*-point spacing of 0.07 Å^{-1}.[57] The Quasi-Newton energy-minimizing approach of Broyden, Fletcher, Goldfarb, and Shanno was used to refine the crystal structures.[58] Structural convergence was assessed using a maximum change in energy of 5×10^{-6} eV atom^{-1}, a maximum displacement of 5×10^{-4} Å atom^{-1}, and a maximum Cartesian force of 10^{-2} eV Å^{-1}. Fixed unit cell parameters were used in all calculations. Where indicated, dispersion was included in the geometry optimiza-

https://dx.doi.org/10.1021/acs.jpca.0c00421
J. Phys. Chem. A 2020, 124, 3109−3119

tions through the two-body force-field method of Grimme (D2)[33,59] or through a modification of that method (D2*).[28,29,36]

Calculations of Magnetic Shielding Tensors. Calculations of ^{13}C and ^{15}N magnetic shielding tensors were performed using both periodic and cluster-based approaches.[37] Periodic calculations employed the GIPAW approach as implemented in CASTEP[12,60] and used the RPBE functional with a plane-wave cutoff energy of 570 eV. Cluster-based calculations employed the Amsterdam Density Functional (ADF 2017) software suite and used the GIAO formalism as implemented in ADF.[61] Clusters of molecules were constructed to represent the extended structures of the solids using the procedures described in previous work.[16,17,20] These calculations employed the PBE0 functional[62,63] and relativistic treatment of the electronic structure at the ZORA scalar level.[63] A basis set partitioning scheme was used, in which the atoms of the central molecule were assigned the TZ2P basis set and all atoms in peripheral molecules were assigned the smaller DZ basis set (Scheme 2).

Statistical Assessment of Data. For each model chemistry, the relationship between calculated principal components of the magnetic shielding tensors ($\sigma_{ii}^{\nu,\text{calc}}$) and experimental principal components of chemical shift tensors ($\delta_{ii}^{\nu,\text{exp}}$) was determined by calculations on a training set of organic crystals (see the Supporting Information for details). Least-squares regression parameters providing the relationship between calculation and experiment were obtained from the expression

$$\sigma_{ii}^{\nu,\text{calc}} = A\delta_{ii}^{\nu,\text{exp}} + B \tag{1}$$

where the index ν denotes the carbon or nitrogen site ($\nu = 1, 2, ..., N$), the index i denotes the principal component of the shielding tensor ($i = 1, 2, 3$), A represents the slope of the correlation line, and B represents the interpolated shielding of the reference system (TMS for ^{13}C shifts and nitromethane for ^{15}N shifts, both at $\delta_{\text{iso}} = 0.0$ ppm for the respective isotopes). Calculated chemical shifts ($\delta_{ii}^{\nu,\text{calc}}$) are obtained from the following expression:

$$\delta_{ii}^{\nu,\text{calc}} = (B - \sigma_{ii}^{\nu,\text{calc}})/|A| \tag{2}$$

The *chemical shift distance* for atom ν, d_ν, is used to compare a calculated and experimental chemical shift tensor with a scalar value (in ppm), given two sets of principal components (see Table 1 for definitions):[64]

$$\begin{aligned} d_\nu = \Big(\frac{1}{15}[&3(\delta_{11}^{\nu,\text{calc}} - \delta_{11}^{\nu,\text{exp}})^2 + 3(\delta_{22}^{\nu,\text{calc}} - \delta_{22}^{\nu,\text{exp}})^2 \\ &+ 3(\delta_{33}^{\nu,\text{calc}} - \delta_{33}^{\nu,\text{exp}})^2 + 2(\delta_{11}^{\nu,\text{calc}} - \delta_{11}^{\nu,\text{exp}})(\delta_{22}^{\nu,\text{calc}} - \delta_{22}^{\nu,\text{exp}}) \\ &+ 2(\delta_{11}^{\nu,\text{calc}} - \delta_{11}^{\nu,\text{exp}})(\delta_{33}^{\nu,\text{calc}} - \delta_{33}^{\nu,\text{exp}}) \\ &+ 2(\delta_{22}^{\nu,\text{calc}} - \delta_{22}^{\nu,\text{exp}})(\delta_{33}^{\nu,\text{calc}} - \delta_{33}^{\text{exp}})]\Big)^{1/2} \end{aligned} \tag{3}$$

A root-mean-square (RMS) chemical shift distance for an ensemble of N chemical shift tensors (Δ_{RMS}) is determined by the following expression:

$$\Delta_{\text{RMS}} = \left(\frac{1}{N}\sum_{\nu=1}^{N} {d_\nu}^2\right)^{1/2} \tag{4}$$

■ RESULTS AND DISCUSSION

Overview. We report the principal components of the ^{13}C chemical shift tensors of the API cimetidine Form A derived from FIREMAT experiments.[51,65] The assignments of the ^{13}C peaks to individual atomic sites is accomplished via DFT calculations of ^{13}C magnetic shielding tensors. We also reassign the ^{15}N peaks of cimetidine using chemical shift tensors reported in a previous study,[7] using DFT calculations of ^{15}N magnetic shielding tensors.

We discuss several considerations for using DFT calculations to aid in chemical shift assignments through calculations of ^{13}C and ^{15}N magnetic shielding tensors for cimetidine and a large training set of organic crystals. First, we evaluate the importance of structural refinement via energy minimization as a prerequisite for accurate calculations of ^{13}C and ^{15}N magnetic shielding tensors. Second, we assess the effect of costlier hybrid DFT methods for the prediction of ^{13}C and ^{15}N magnetic shielding tensors, with an emphasis on the discrepancies associated with the prediction of ^{13}C magnetic shielding tensors of carbon atoms bound to nitrogen. The assignments of the ^{13}C and ^{15}N peaks of cimetidine Form A are accomplished using the combination of these methods that leads to the best agreement between experiment and theory, which includes geometry optimization at the RPBE-D2* level and calculation of the magnetic shielding tensors at the PBE0 level (*vide infra*). Complete lists of all calculated values are found in Tables S2 and S3.

Assignment of the ^{13}C Chemical Shifts of Cimetidine. The polymorphs of cimetidine display large variations in the carbon chemical shifts due to differences among the crystal structures; these largely arise due to variations in the inter- and intramolecular hydrogen-bonding networks in each solid form and the number of crystallographically distinct molecules in the asymmetric units.[39] The 14.1 T high-resolution ^{13}C SSNMR spectrum of cimetidine Form A features resolved peaks for many of the ten ^{13}C resonances (Figure 1); exceptions include the two

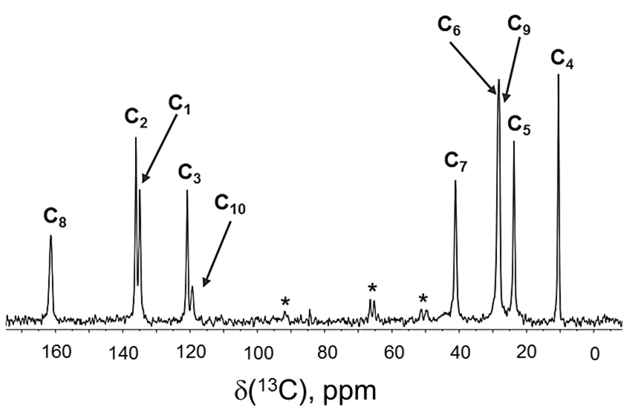

Figure 1. High-resolution ^{1}H−^{13}C CP/MAS spectrum of cimetidine Form A acquired at 14.1 T with $\nu_{\text{rot}} = 10.5$ kHz. Spinning sidebands are marked by asterisks.

overlapping peaks at *ca.* 28 ppm and the peaks at 119.2 and 134.8 ppm that are broadened by ^{13}C−^{14}N residual dipolar coupling.[66−68] Dipolar-dephased spectra (9.4 T) differentiate the CH_2 group of position C_6 from the methyl C_9 and the protonated C_1 position from the quaternary C_2 (Figure S1).

Three pairs of carbon atoms (C_3/C_{10}, C_1/C_2, and C_6/C_9) have isotropic shifts that differ by only 1.5, 1.0, and 0.5 ppm,

https://dx.doi.org/10.1021/acs.jpca.0c00421
J. Phys. Chem. A 2020, 124, 3109−3119

respectively. Because the accuracy of DFT calculations of isotropic ^{13}C chemical shifts is currently around ±2 ppm,[16−19,21,69] assignments using calculations of these values alone cannot be relied upon. Even the most accurate computational protocol considered herein (as judged through calculations of ^{13}C and ^{15}N magnetic shielding tensors of the training set) is unable to predict the correct assignments of the isotropic chemical shifts of the C_3/C_{10} pair (Table 1). In addition, this assignment error is not detected by dipolar dephasing experiments because both carbon atoms are identified as quaternary.

The principal components of the ^{13}C chemical shift tensors for the ten carbon sites were determined by analysis of the spinning sidebands in the FIREMAT spectrum (Figure 2). The FIREMAT spectrum was acquired at 14.1 T to help suppress the ^{13}C−^{14}N residual dipolar coupling (see Figure S2, which compares ^{1}H−^{13}C CP/MAS spectra obtained at 9.4 and 14.1 T). Previous work has compared the principal components of ^{13}C chemical shift tensors obtained by FIREMAT with those obtained from single-crystal studies; this analysis concluded that the errors in individual principal components obtained from FIREMAT data are ±0.7 ppm.[65] The measurement of the ^{13}C chemical shift tensor components, along with DFT calculations of the same values, enabled the assignment of all peaks to the appropriate carbon sites with a high degree of statistical confidence, resulting in a Δ_{RMS}(^{13}C) of 3.3 ppm (*vide infra*). The six ^{15}N peaks of cimetidine Form A were also assigned unambiguously using DFT calculations of the ^{15}N chemical shift tensors, resulting in a Δ_{RMS}(^{15}N) of 5.7 ppm (Table 2).

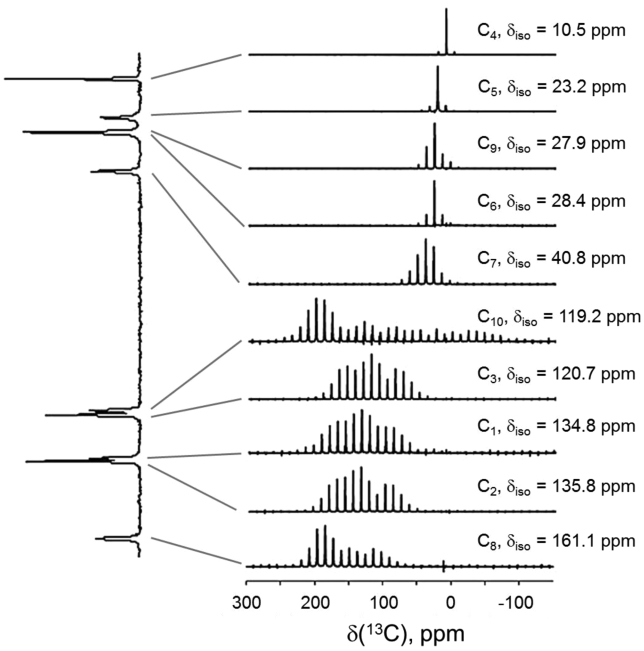

Figure 2. ^{13}C FIREMAT spectrum of cimetidine Form A acquired at 14.1 T.

Measurement of the principal components of the ^{13}C chemical shift tensors allowed C_3 and C_{10} to be assigned readily, even though these sites could not be assigned unambiguously from the isotropic peaks and dipolar-dephased spectra (*cf.* Figure 2 and Figure S1). Interestingly, the two most similar ^{13}C chemical shift tensors correspond to the nitrogen-bonded methyl carbon C_9 and the methylene carbon C_6; the corresponding principal components differ by $\Delta\delta_{11}$ = 1.2 ppm, $\Delta\delta_{22}$ = 3.5 ppm, and $\Delta\delta_{33}$ = 5.6 ppm. The tensors corresponding to imidazole ring carbons C_1 and C_2 are also similar, with the individual values differing by $\Delta\delta_{11}$ = 4.9 ppm, $\Delta\delta_{22}$ = 5.9 ppm, and $\Delta\delta_{33}$ = 2.0 ppm. The assignment (Table 1) is consistent with the dipolar-dephased spectra, which differentiate the methylene C_6 from the methyl C_9 and the protonated C_1 from the quaternary C_2.

Because of the high certainty with which the chemical shifts in cimetidine Form A can be assigned, we use calculations on this solid to assess factors affecting the accuracies of calculations of magnetic shielding tensors. These observations are strengthened by calculations on a training set of organic solids in which the peak assignments are not in question, due to (i) the small number of unique carbon or nitrogen atoms in the crystal structures and/or (ii) the availability of single-crystal NMR data.

Geometry Optimizations. Calculations of ^{13}C and ^{15}N magnetic shielding tensors display a dependence on the type of structural data used in the calculation (*e.g.*, XRD-derived structures *vs.* structures refined with plane-wave DFT calculations).[70] We have considered several geometry optimization protocols to refine the crystal structures of cimetidine and the structures of the training set (Figure 3, Table 3). Four types of structural data are evaluated, including (i) structures

Table 2. Experimental and Calculated Principal Components of the ^{15}N Chemical Shift Tensors of Cimetidine Form A[a,b]

nitrogen no.		δ_{iso} (ppm)	Ω (ppm)	κ	δ_{11} (ppm)	δ_{22} (ppm)	δ_{33} (ppm)
1	exp	−209.9	161.7	0.11	−132.0	−204.0	−293.7
	calc	−212.2	185.5	0.01	−119.7	−211.6	−305.2
2	exp	−127.4	377.4	0.50	30.1	−65.1	−347.3
	calc	125.2	390.5	0.49	38.4	−61.8	−352.2
3	exp	−283.9	95.8	−1.00	−220.0	−315.8	−315.8
	calc	−279.7	106.5	−0.90	−210.5	−311.7	−317.0
4	exp	−297.1	124.4	−0.60	−222.5	−321.9	−346.9
	calc	−300.6	102.0	−0.84	−235.4	−329.1	−337.4
5	exp	−294.7	83.3	−0.15	−250.9	−298.9	−334.2
	calc	−290.6	83.2	−0.18	−246.5	−295.6	−329.6
6	exp	−190.5	308.2	0.62	−68.0	−127.3	−376.2
	calc	−184.5	310.0	0.57	−58.9	−125.6	−368.9

[a]Experimental values are taken from ref 7. These values were originally referenced to neat ammonia, which is at −380.2 ppm relative to nitromethane. Calculated values were obtained from calculation on a structure refined at the RPBE-D2* level. The magnetic shielding tensors were calculated at the PBE0/TZ2P level. [b]See Table 1 for definitions of chemical shift tensor parameters.

https://dx.doi.org/10.1021/acs.jpca.0c00421
J. Phys. Chem. A 2020, 124, 3109−3119

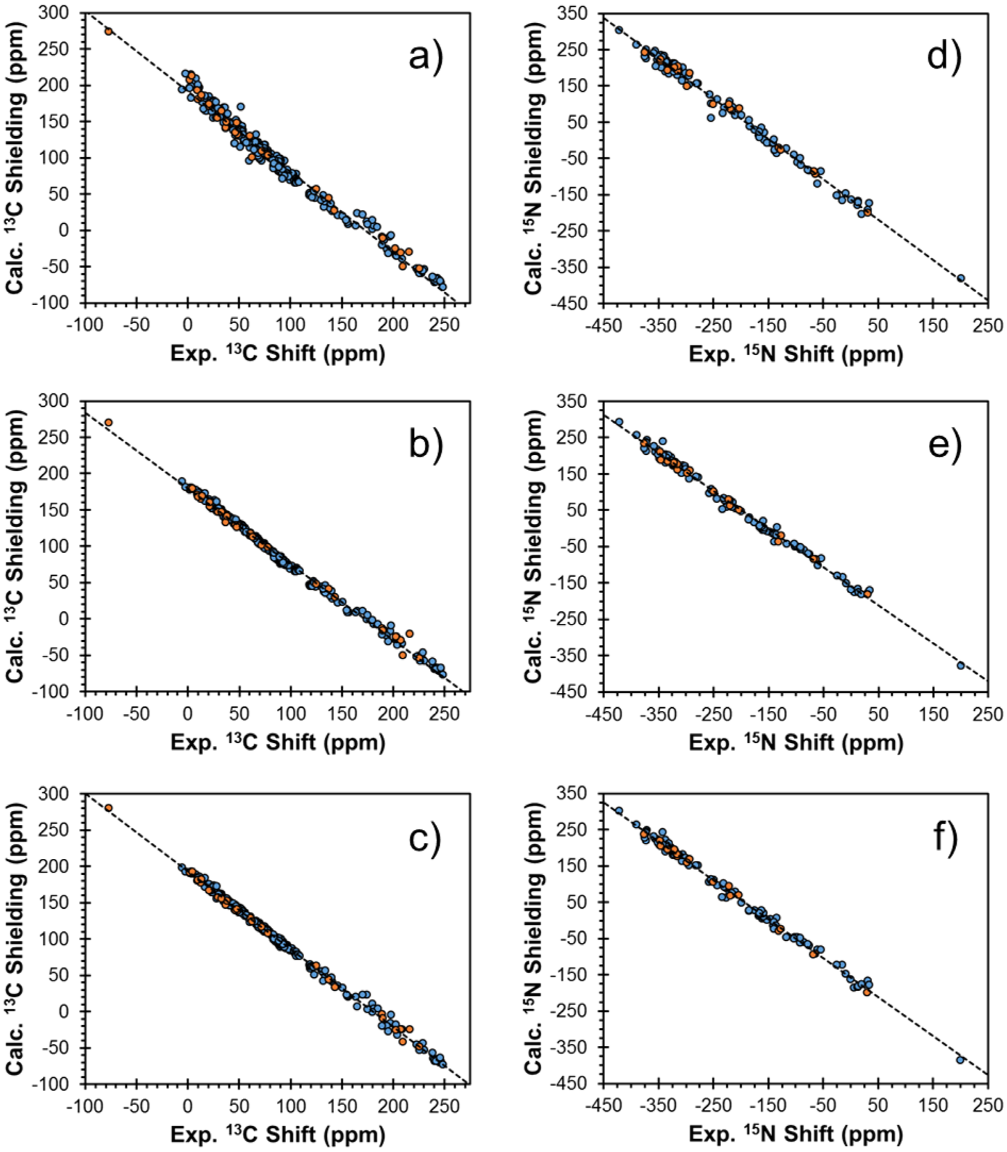

Figure 3. Comparison between calculated principal components of magnetic shielding tensors and experimental principal components of chemical shift tensors. Values are illustrated for ^{13}C sites in panels a−c and for ^{15}N sites in panels d−f. Calculations were performed on structures obtained from X-ray diffraction methods (a, d) or on structures refined at the RPBE D2* level (b, c, e, f). Magnetic shielding tensors were calculated at either the RPBE level (a, b, d, e) or the PBE0 level (c, f). Points shown in blue and orange correspond to the training set and cimetidine, respectively. Plots of ^{13}C shielding tensors display 339 points, whereas plots of ^{15}N shielding tensors display 132 points.

obtained from SCXRD and refined structures obtained by plane-wave DFT energy-minimizations at the (ii) RPBE, (iii) RPBE-D2, and (iv) RPBE-D2* levels.

The DFT-D2* model uses a reparametrization of the D2 force field that is optimized to improve calculations of NMR parameters in organic solids.[28,29,36] Although other classes of dispersion corrections are available,[34,35] we have demonstrated that two-body models such as D2 can be optimized readily using input from experimental determinations of nuclear EFG tensors. Previously, this was accomplished by modulating the value of the damping parameter (d) in the D2 force field in a series of DFT geometry optimizations and gauging the validity of the resulting structures through comparison of calculated and experimental EFG tensor parameters. Here, we follow a similar approach, in which calculations of ^{13}C and ^{15}N magnetic shielding tensors of the training set crystals were performed following a series of geometry optimizations in which the value of the damping parameter was varied (Figure S3 and Table S4). The prediction of ^{15}N magnetic shielding parameters is improved by setting the value of the damping parameter to low values, with $\Delta_{RMS}(^{15}N)$ decreasing continuously over the range $3.0 \leq d \leq 10.0$ (the lowest value was obtained when $d = 3.0$). In contrast, $\Delta_{RMS}(^{13}C)$ is unaffected by the choice of the damping parameter when $d \geq 5.0$; below this value, $\Delta_{RMS}(^{13}C)$ increases. This difference in behavior between carbon and nitrogen magnetic shielding tensors likely reflects the fact that nitrogen atoms commonly participate in intermolecular noncovalent interactions, which results in magnetic shielding tensors that are more strongly influenced by long-range interactions. On the basis of the comparison of the ^{13}C and ^{15}N calculations, the value of the damping parameter was set to $d = 5.0$ in all subsequent RPBE-D2* energy minimizations, since calculations performed with this value of d work well for prediction of both quantities.

https://dx.doi.org/10.1021/acs.jpca.0c00421
J. Phys. Chem. A 2020, 124, 3109−3119

Table 3. Statistical Data Associated with the Predictions of ^{13}C and ^{15}N Magnetic Shielding Tensors for Cimetidine and the Training Set

			training set				cimetidine
atom	geometry[a]	shielding[b]	N[c]	σ_{ref} (ppm)[d]	slope	Δ_{RMS} (ppm)[e]	Δ_{RMS} (ppm)
carbon	XRD	RPBE	96	192.1	−1.111	6.8	7.5
	RPBE	RPBE	103	174.5	−1.032	3.2	5.0
	RPBE-D2	RPBE	103	173.8	−1.030	3.2	5.1
	RPBE-D2*	RPBE	103	179.3	−1.043	3.2	4.8
	RPBE-D2*	PBE0	103	193.4	−1.074	2.3	3.3
nitrogen	XRD	RPBE	33	−163.6	−1.112	10.9	10.3
	RPBE	RPBE	38	−163.8	−1.042	7.8	6.9
	RPBE-D2	RPBE	38	−164.3	−1.042	7.9	6.6
	RPBE-D2*	RPBE	38	−159.2	−1.049	7.5	5.8
	RPBE-D2*	PBE0	38	−157.6	−1.075	7.1	5.7

[a]Refers to the type of structural data used in the calculations, *i.e.*, structures determined from X-ray diffraction or one of several plane-wave DFT methods. [b]Refers to the functional used in the calculations of the magnetic shielding tensors. Calculations were performed either using CASTEP (GIPAW) with the RPBE functional or using ADF (GIAO) with the PBE0 functional. [c]*N* refers to the number of shielding tensors in the training set; this value is lower for the XRD-derived structures because the positions of the hydrogen atoms were not always reported. [d]σ_{ref} refers to the shielding of the reference compound (*i.e.*, TMS and nitromethane for the ^{13}C and ^{15}N training sets, respectively). [e]Δ_{RMS} refers to the root-mean-square chemical shift distance (see eqs 3 and 4 for definitions).

The effects of structural refinement are evident in the calculations of ^{13}C and ^{15}N magnetic shielding tensors in cimetidine and the training set (Table 3). For the training set of 103 ^{13}C shielding tensors, calculations on structures derived from SCXRD measurements yields a Δ_{RMS}(^{13}C) of 6.8 ppm. When these structures are refined using DFT calculations, Δ_{RMS}(^{13}C) falls to 3.2 ppm, independent of the energy-minimization protocol. Similarly, calculations using the SCXRD structure of cimetidine leads to a Δ_{RMS}(^{13}C) of 7.5 ppm, whereas this value for the refined structures ranges between 4.8 and 5.1 ppm. The results for cimetidine with the lowest Δ_{RMS}(^{13}C) of 4.8 ppm are obtained for structures refined at the RPBE-D2* level. For the training set of 38 ^{15}N magnetic shielding tensors, calculations involving the experimental SCXRD structures result in a Δ_{RMS}(^{15}N) of 10.9 ppm, whereas those values for the refined structures range between 7.5 and 7.8 ppm. Cimetidine follows this trend, with the calculations using the SCXRD structure resulting in an Δ_{RMS}(^{15}N) of 10.3 ppm, and those on refined structures having values of Δ_{RMS}(^{15}N) between 5.8 and 6.9 ppm. For both the training set and cimetidine, the best agreement with experimental ^{15}N chemical shift tensors is obtained from structures refined at the RPBE-D2* level.

Structural refinement has a direct impact on the assignment of the ^{13}C peaks for cimetidine. Calculations of ^{13}C magnetic shielding tensors for structures obtained using any of the three geometry optimization protocols result in the same assignment of the ^{13}C peaks, with values for Δ_{RMS}(^{13}C) below 5.1 ppm in all cases. ^{13}C magnetic shielding tensor parameters obtained from calculations on the SCXRD-derived structure do not allow for the correct assignment of peaks, due to the high Δ_{RMS}(^{13}C) associated with any possible assignment; even the correct peak assignments yield a higher Δ_{RMS}(^{13}C) of 7.5 ppm. The importance of accurate positioning of hydrogen atoms is particularly evident from calculations of the shielding tensors of the C_4 and C_9 methyl carbons. For structures derived from SCXRD, these sites feature values of d_v of 10.2 and 14.0 ppm, respectively; however, refinement at the RPBE-D2* level reduces these values to only 1.2 and 2.3 ppm, respectively (Table S2). Improvement is also seen in the calculation of nonprotonated imidazole carbon C_2, for which d_v reduces from 9.0 to 3.0 ppm following refinement.

Evaluation of DFT Functionals. In addition to their dependences on molecular-level structure, DFT calculations of ^{13}C and ^{15}N magnetic shielding tensors depend on the choice of exchange−correlation functional (Figure 3, Table 3, Tables S5 and S6). Because several of the ^{13}C magnetic shielding tensors in cimetidine proved difficult to predict using the GGA RPBE functional (Δ_{RMS}(^{13}C) = 4.8 ppm), it is plausible that calculations of the ^{13}C magnetic shielding tensors could be improved by more advanced DFT techniques, *i.e.*, a hybrid DFT method. The superior agreement with experiment that is often afforded by hybrid DFT functionals is sometimes rationalized by the ability of these methods to provide better descriptions of interactions between occupied and virtual orbitals, which greatly impact paramagnetic contributions to the individual principal components of shielding tensors.[71,72]

To investigate this, the ^{13}C and ^{15}N shielding values for the RPBE-D2* structures (cimetidine and training set) were calculated with the hybrid PBE0 functional (which introduces a 25% admixture of HFX), a Slater-type basis set, and cluster-based models of the extended lattice structure. There are differences between the results obtained with the RPBE and PBE0 functionals, as indicated by the variation in the slopes of the linear regression lines (A), the interpolated values for the shielding of the reference compounds (B), and the values of Δ_{RMS}(^{13}C) or Δ_{RMS}(^{15}N). The use of the hybrid functional PBE0 leads to more shielded values of B, as well as values of A with magnitudes that deviate more from unity. For the training set of ^{15}N shielding tensors, Δ_{RMS}(^{15}N) is reduced marginally from 7.5 ppm (RPBE) to 7.1 ppm (PBE0). The choice of functional seems to have little effect on the accuracy of the predictions of ^{15}N magnetic shielding tensors in cimetidine; a value for Δ_{RMS}(^{15}N) of 5.8 ppm is obtained from the RPBE functional, and 5.7 ppm for the PBE0 functional. For the training set of ^{13}C shielding tensors, Δ_{RMS}(^{13}C) is reduced from 3.2 ppm (RPBE) to 2.3 ppm (PBE0). For cimetidine, Δ_{RMS}(^{13}C) is reduced from 4.8 ppm (RPBE) to 3.3 ppm (PBE0). This improvement (Table S2) is due largely to the calculation of the shielding tensor of C_8, a guanidine-type carbon; here, d_v is reduced from 11.6 ppm (RPBE) to 5.9 ppm (PBE0). Substantial

https://dx.doi.org/10.1021/acs.jpca.0c00421
J. Phys. Chem. A 2020, 124, 3109−3119

reductions in d_v are also observed for the protonated imidazole carbon C_1 (5.2 ppm to 2.3 ppm) and the nitrile carbon C_{10} (5.4 ppm to 3.7 ppm).

Although the benefits afforded by hybrid functionals extend to the prediction of the shielding tensors of all types of carbon atoms, the largest effects are seen for those that are bound to nitrogen atoms (Table 4). For the training set, calculations at the RPBE level result in $\Delta_{RMS}(^{13}C)$ of 4.6 ppm for carbon atoms bound to nitrogen, and only 2.9 ppm for all other carbon atoms. Calculations at the PBE0 level result in $\Delta_{RMS}(^{13}C)$ of 3.2 ppm for carbon atoms bound to nitrogen and 2.2 ppm for all other carbon atoms. Thus, the differences in $\Delta_{RMS}(^{13}C)$ among these subpopulations of carbon species are reduced when a hybrid functional is employed for the calculation of the magnetic shielding tensors. Calculations employing hybrid functionals also remove systematic discrepancies between magnetic shielding tensors of carbon atoms featuring different hybridization states (*i.e.*, sp, sp^2, and sp^3 carbons).[17] In particular, calculations performed using hybrid functionals result in higher shielding constants for sp^3-hybridized carbons, relative to the results obtained using a comparable GGA functional (*e.g.*, PBE0 versus PBE), whereas the use of hybrid functionals leads to nuclear shielding or deshielding of sp- and sp^2-hybridized carbons, depending on the particular chemical environment and the principal component (*i.e.*, σ_{11} and σ_{22} are not affected systematically, whereas σ_{33} is shielded in a similar manner to sp^3-hybridized carbons).[17] It is possible that the larger values of $\Delta_{RMS}(^{13}C)$ associated with carbon atoms bound to nitrogen reflect the differences in the bonding arrangements and local symmetry environments of these sites. Additionally, most of the carbon atoms in cimetidine are bound to one or more nitrogen atom. Because of this, the values of $\Delta_{RMS}(^{13}C)$ observed for cimetidine are higher than those for the training set, independent of the type of structural data or DFT functional used in the calculations. However, use of the hybrid functional, PBE0, brings calculated shielding tensors into closer agreement with experiment. The improved correlation results largely from the calculations of the shielding tensors of C_1, C_8, and C_{10} (C_1 and C_{10} are bound to two nitrogen atoms, whereas C_8 is bound to three nitrogen atoms; additionally, C_1 and C_8 are both sp^2-hybridized whereas C_{10} is sp-hybridized).

Table 4. Chemical Shift Distances for Carbon Sites Either Bonded or Not Bonded to a Nitrogen atom

		Δ_{RMS} (ppm)	
geometry[a]	shielding[b]	bonded to nitrogen	not bonded to nitrogen
XRD	RPBE	6.6	6.9
RPBE	RPBE	4.8	3.0
RPBE-D2	RPBE	4.9	3.0
RPBE-D2*	RPBE	4.6	2.9
RPBE-D2*	PBE0	3.2	2.2

[a]Refers to the type of structural data used in the calculations, *i.e.*, structures determined from X-ray diffraction or one of several plane-wave DFT methods. [b]Refers to the functional used in the calculations of the magnetic shielding tensors. Calculations were performed either using CASTEP (GIPAW) with the RPBE functional or using ADF (GIAO) with the PBE0 functional.

CONCLUSIONS

The principal components of the ^{13}C chemical shift tensors of cimetidine Form A were measured by the FIREMAT experiment and modeled with DFT calculations to provide an unambiguous assignment of the carbon spectrum. Peak assignments based solely on calculations of isotropic shifts lead to erroneous results that are not detected by measuring dipolar-dephased spectra. However, measurements of the chemical shift tensors allow the peaks to be assigned while also providing a data set rich in electronic structural information that is indispensable to NMR crystallographic investigations.

The effects of various types of structural refinement using plane-wave DFT were explored. In particular, a semiempirical force field was reparameterized to refine the structures of organic crystals, leading to enhanced predictions of ^{15}N magnetic shielding tensors for nitrogen atoms in many types of chemical environments, and sometimes to small improvement in the prediction of ^{13}C magnetic shielding tensors.

The use of hybrid functionals leads to improvement in the calculation of ^{13}C and ^{15}N magnetic shielding tensors. Accurate prediction of the principal components of ^{13}C and ^{15}N chemical shift tensors in organic molecules is challenging. In the literature, it is not uncommon to find large discrepancies between experimental data when calculations are limited to GGA-type functionals. At the GGA level, the ^{13}C $\Delta_{RMS}(^{13}C)$ of cimetidine is significantly larger than that of the training set of organic solids (4.8 ppm compared to 3.2 ppm). Moreover, calculations of the ^{13}C magnetic shielding tensors of carbon atoms bound to nitrogen have larger $\Delta_{RMS}(^{13}C)$ values than for those of carbons atoms bound to other types of atoms. This difficulty is partially alleviated using hybrid functionals.

ASSOCIATED CONTENT

Supporting Information

The Supporting Information is available free of charge at https://pubs.acs.org/doi/10.1021/acs.jpca.0c00421.

Summaries of materials used in calculations, of shift tensors calculations, CP/MAS spectra, variation of Δ_{RMS} values, and magnetic shielding tensor calculation results (PDF)

Energy-minimized crystal structures (.cif) and clusters (.xyz) and output files from ADF (.log) and CASTEP (.magres) magnetic shielding calculations (ZIP)

AUTHOR INFORMATION

Corresponding Authors

Robert W. Schurko − *Department of Chemistry & Biochemistry, Florida State University, Tallahassee, Florida 32306, United States*; orcid.org/0000-0002-5093-400X; Phone: (724)-503-1001 x6132; Email: riuliucci@washjeff.edu

Robbie J. Iuliucci − *Department of Chemistry, Washington and Jefferson College, Washington, Pennsylvania 15301, United States*; Phone: (850) 645-8614; Email: rschurko@fsu.edu

Authors

Sean T. Holmes − *Department of Chemistry & Biochemistry, Florida State University, Tallahassee, Florida 32306, United States*

Olivia G. Engl − *Department of Chemistry, Washington and Jefferson College, Washington, Pennsylvania 15301, United States*

Matthew N. Srnec − *Department of Chemistry, Physics, & Engineering, Franciscan University, Steubenville, Ohio 43952, United States*; orcid.org/0000-0001-5386-1603

https://dx.doi.org/10.1021/acs.jpca.0c00421
J. Phys. Chem. A 2020, 124, 3109−3119

¶Jeffry D. Madura – Department of Chemistry & Biochemistry, Center for Computational Sciences, Duquesne University, Pittsburgh, Pennsylvania 15282, United States
Rosalynn Quiñones – Department of Chemistry, Marshall University, Huntington, West Virginia 25755, United States; orcid.org/0000-0001-8455-4358
James K. Harper – Department of Chemistry & Biochemistry, Brigham Young University, Provo, Utah 84602, United States

Complete contact information is available at: https://pubs.acs.org/10.1021/acs.jpca.0c00421

Notes

The authors declare no competing financial interest.
¶Deceased 14 March 2017.

■ ACKNOWLEDGMENTS

S.T.H. and R.W.S. thank Genentech, the Natural Sciences and Engineering Research Council of Canada (Discovery Grant, RGPIN-2016-06642), the Canadian Foundation for Innovation, the Ontario Innovation Trust, the University of Windsor, Florida State University, and the National High Magnetic Field Laboratory for funding this research. The National High Magnetic Field Laboratory is supported by the National Science Foundation through NSF/DMR-1644779* and the State of Florida. R.J.I. and O.G.E. were supported by the National Science Foundation (NSF/REU CHE-1659821, NSF/MRI CHE-1726824, and CHE-1126465). J.K.H. was supported by the National Science Foundation through NSF/CHE-2016185. This work was also supported by the Shared Hierarchical Academic Research Computing Network (SHARCNET: http://www.sharcnet.ca).

■ REFERENCES

(1) Massiot, D.; Fayon, F.; Capron, M.; King, I.; Le Calvé, S.; Alonso, B.; Durand, J.-O.; Bujoli, B.; Gan, Z.; Hoatson, G. Modelling one- and two-dimensional solid-state NMR spectra. *Magn. Reson. Chem.* **2002**, *40*, 70−76.
(2) Ashbrook, S. E.; McKay, D. Combining solid-state NMR spectroscopy with first-principles calculations - a guide to NMR crystallography. *Chem. Commun.* **2016**, *52*, 7186−7204.
(3) Harris, R. K.; Wasylishen, R. E.; Duer, M. J. *NMR Crystallography*; John Wiley & Sons Ltd.: Singapore, 2009.
(4) Harper, J. K.; Iuliucci, R. J. ^{13}C Chemical-Shift Tensors in Organic Materials. *Encyclopedia of Analytical Chemistry*; Wiley, 2014.
(5) Iuliucci, R. J.; Clawson, J.; Hu, J. Z.; Solum, M. S.; Barich, D.; Grant, D. M.; Taylor, C. M. V. Ring-chain tautomerism in solid-phase erythromycin A: evidence by solid-state NMR. *Solid State Nucl. Magn. Reson.* **2003**, *24*, 23−38.
(6) Harper, J. K.; Iuliucci, R.; Gruber, M.; Kalakewich, K. Refining crystal structures with experimental ^{13}C NMR shift tensors and lattice-including electronic structure methods. *CrystEngComm* **2013**, *15*, 8693−8704.
(7) Kalakewich, K.; Iuliucci, R.; Mueller, K. T.; Eloranta, H.; Harper, J. K. Monitoring the refinement of crystal structures with ^{15}N solid-state NMR shift tensor data. *J. Chem. Phys.* **2015**, *143*, 194702.
(8) Holmes, S. T.; Wang, W. D.; Hou, G.; Dybowski, C.; Wang, W.; Bai, S. A new NMR crystallographic approach to reveal the calcium local structure of atorvastatin calcium. *Phys. Chem. Chem. Phys.* **2019**, *21*, 6319−6326.
(9) Wang, W. D.; Gao, X. D.; Strohmeier, M.; Wang, W.; Bai, S.; Dybowski, C. Solid-state NMR studies of form I of atorvastatin calcium. *J. Phys. Chem. B* **2012**, *116*, 3641−3649.
(10) Carignani, E.; Borsacchi, S.; Marini, A.; Mennucci, B.; Geppi, M. ^{13}C chemical shielding tensors: A combined solid-state NMR and DFT study of the role of small-amplitude motions. *J. Phys. Chem. C* **2011**, *115*, 25023−25029.
(11) Charpentier, T. The PAW/GIPAW approach for computing NMR parameters: a new dimension added to NMR study of solids. *Solid State Nucl. Magn. Reson.* **2011**, *40*, 1−20.
(12) Bonhomme, C.; Gervais, C.; Babonneau, F.; Coelho, C.; Pourpoint, F.; Azais, T.; Ashbrook, S. E.; Griffin, J. M.; Yates, J. R.; Mauri, F.; Pickard, C. J. First-principles calculation of NMR parameters using the gauge including projector augmented wave method: a chemist's point of view. *Chem. Rev.* **2012**, *112*, 5733−5779.
(13) Beran, G. J.; Hartman, J. D.; Heit, Y. N. Predicting molecular crystal properties from first principles: finite-temperature thermochemistry to NMR crystallography. *Acc. Chem. Res.* **2016**, *49*, 2501−2508.
(14) Hartman, J. D.; Day, G. M.; Beran, G. J. O. Enhanced NMR discrimination of pharmaceutically relevant molecular crystal forms through fragment-based ab initio chemical shift predictions. *Cryst. Growth Des.* **2016**, *16*, 6479−6493.
(15) Tatton, A. S.; Blade, H.; Brown, S. P.; Hodgkinson, P.; Hughes, L. P.; Lill, S. O. N.; Yates, J. R. Improving confidence in crystal structure solutions using NMR crystallography: the case of β-piroxicam. *Cryst. Growth Des.* **2018**, *18*, 3339−3351.
(16) Holmes, S. T.; Iuliucci, R. J.; Mueller, K. T.; Dybowski, C. Density functional investigation of intermolecular effects on ^{13}C NMR chemical-shielding tensors modeled with molecular clusters. *J. Chem. Phys.* **2014**, *141*, 164121.
(17) Holmes, S. T.; Iuliucci, R. J.; Mueller, K. T.; Dybowski, C. Critical analysis of cluster models and exchange-correlation functionals for calculating magnetic shielding in molecular solids. *J. Chem. Theory Comput.* **2015**, *11*, 5229−5241.
(18) Hartman, J. D.; Monaco, S.; Schatschneider, B.; Beran, G. J. O. Fragment-based ^{13}C nuclear magnetic resonance chemical shift predictions in molecular crystals: an alternative to planewave methods. *J. Chem. Phys.* **2015**, *143*, 102809.
(19) Hartman, J. D.; Kudla, R. A.; Day, G. M.; Mueller, L. J.; Beran, G. J. O. Benchmark fragment-based ^{1}H, ^{13}C, ^{15}N and ^{17}O chemical shift predictions in molecular crystals. *Phys. Chem. Chem. Phys.* **2016**, *18*, 21686−21709.
(20) Alkan, F.; Holmes, S. T.; Dybowski, C. Role of exact exchange and relativistic approximations in calculating ^{19}F magnetic shielding in solids using a cluster ansatz. *J. Chem. Theory Comput.* **2017**, *13*, 4741−4752.
(21) Hartman, J. D.; Beran, G. J. O. Accurate ^{13}C and ^{15}N molecular crystal chemical shielding tensors from fragment-based electronic structure theory. *Solid State Nucl. Magn. Reson.* **2018**, *96*, 10−18.
(22) Dracinsky, M.; Unzueta, P.; Beran, G. J. O. Improving the accuracy of solid-state nuclear magnetic resonance chemical shift prediction with a simple molecular correction. *Phys. Chem. Chem. Phys.* **2019**, *21*, 14992−15000.
(23) Hartman, J. D.; Balaji, A.; Beran, G. J. O. Improved electrostatic embedding for fragment-based chemical shift calculations in molecular crystals. *J. Chem. Theory Comput.* **2017**, *13*, 6043−6051.
(24) Hodgkinson, P. NMR Crystallography of Molecular Organics. *Prog. Nucl. Magn. Reson. Spectrosc.* **2020**, DOI: 10.1016/j.pnmrs.2020.03.001
(25) Baias, M.; Dumez, J. N.; Svensson, P. H.; Schantz, S.; Day, G. M.; Emsley, L. De novo determination of the crystal structure of a large drug molecule by crystal structure prediction-based powder NMR crystallography. *J. Am. Chem. Soc.* **2013**, *135*, 17501−17507.
(26) Widdifield, C. M.; Farrell, J. D.; Cole, J. C.; Howard, J. A. K.; Hodgkinson, P. Resolving alternative organic crystal structures using density functional theory and NMR chemical shifts. *Chem. Sci.* **2020**, *11*, 2987.
(27) Webber, A. L.; Emsley, L.; Claramunt, R. M.; Brown, S. P. NMR crystallography of campho[2,3-c]pyrazole ($Z' = 6$): combining high-resolution ^{1}H-^{13}C solid-state MAS NMR spectroscopy and GIPAW chemical-shift calculations. *J. Phys. Chem. A* **2010**, *114*, 10435−10442.
(28) Holmes, S. T.; Iuliucci, R. J.; Mueller, K. T.; Dybowski, C. Semi-empirical refinements of crystal structures using ^{17}O quadrupolar-coupling tensors. *J. Chem. Phys.* **2017**, *146*, 064201.

(29) Holmes, S. T.; Schurko, R. W. Refining crystal structures with quadrupolar NMR and dispersion-corrected density functional theory. *J. Phys. Chem. C* **2018**, *122*, 1809−1820.

(30) Kalakewich, K.; Iuliucci, R.; Harper, J. K. Establishing accurate high-resolution crystal structures in the absence of diffraction data and single crystals—an NMR approach. *Cryst. Growth Des.* **2013**, *13*, 5391−5396.

(31) Wang, L.; Uribe-Romo, F. J.; Mueller, L. J.; Harper, J. K. Predicting anisotropic thermal displacements for hydrogens from solid-state NMR: a study on hydrogen bonding in polymorphs of palmitic acid. *Phys. Chem. Chem. Phys.* **2018**, *20*, 8475−8487.

(32) Powell, J.; Kalakewich, K.; Uribe-Romo, F. J.; Harper, J. K. Solid-state NMR and DFT predictions of differences in COOH hydrogen bonding in odd and even numbered n-alkyl fatty acids. *Phys. Chem. Chem. Phys.* **2016**, *18*, 12541−12549.

(33) Grimme, S. Semiempirical GGA-type density functional constructed with a long-range dispersion correction. *J. Comput. Chem.* **2006**, *27*, 1787−1799.

(34) Hoja, J.; Reilly, A. M.; Tkatchenko, A. First-principles modeling of molecular crystals: structures and stabilities, temperature and pressure. *WIREs Comput. Mol. Sci.* **2017**, *7*, No. e1294.

(35) Grimme, S. Density functional theory with London dispersion corrections. *Wiley Interdiscip. Rev.: Comput. Mol. Sci.* **2011**, *1*, 211−228.

(36) Peach, A. A.; Hirsh, D. A.; Holmes, S. T.; Schurko, R. W. Mechanochemical syntheses and ^{35}Cl solid-state NMR characterization of fluoxetine HCl cocrystals. *CrystEngComm* **2018**, *20*, 2780−2792.

(37) Beran, G. J. O. Modeling polymorphic molecular crystals with electronic structure theory. *Chem. Rev.* **2016**, *116*, 5567−5613.

(38) Quirke, V. Putting theory into practice: James Black, receptor theory and the development of the beta-blockers at ICI, 1958−1978. *Med. Hist.* **2006**, *50*, 69−92.

(39) Middleton, D. A.; Le Duff, C. S.; Berst, F.; Reid, D. G. A cross-polarization magic-angle spinning ^{13}C NMR characterization of the stable solid-state forms of cimetidine. *J. Pharm. Sci.* **1997**, *86*, 1400−1402.

(40) Watts, A. E.; Maruyoshi, K.; Hughes, C. E.; Brown, S. P.; Harris, K. D. M. Combining the advantages of powder X-ray diffraction and NMR crystallography in structure determination of the pharmaceutical material cimetidine hydrochloride. *Cryst. Growth Des.* **2016**, *16*, 1798−1804.

(41) Pacilio, J. E.; Tokarski, J. T.; Quiñones, R.; Iuliucci, R. J. High-resolution solid-state NMR spectroscopy: characterization of polymorphism in cimetidine, a pharmaceutical compound. *J. Chem. Educ.* **2014**, *91*, 1236−1239.

(42) Middleton, D. A.; Le Duff, C. S.; Peng, X.; Reid, D. G.; Saunders, D. Molecular conformations of the polymorphic dorms of cimetidine from ^{13}C solid-state NMR distance and angle measurements. *J. Am. Chem. Soc.* **2000**, *122*, 1161−1170.

(43) Middleton, D. A.; Peng, X.; Saunders, D.; Shankland, K.; David, W. I. F.; Markvardsen, A. J. Conformational analysis by solid-state NMR and its application to restrained structure determination from powder diffraction data. *Chem. Commun.* **2002**, 1976−1977.

(44) Madine, J.; Middleton, D. A. An NMR strategy for obtaining multiple conformational constraints for ^{15}N−^{13}C spin-pair labelled organic solids. *Phys. Chem. Chem. Phys.* **2006**, *8*, 5223−5228.

(45) Maruyoshi, K.; Iuga, D.; Watts, A. E.; Hughes, C. E.; Harris, K. D. M.; Brown, S. P. Assessing the detection limit of a minority solid-state form of a pharmaceutical by ^{1}H double-quantum magic-angle spinning nuclear magnetic resonance spectroscopy. *J. Pharm. Sci.* **2017**, *106*, 3372−3377.

(46) Quiñones, R.; Iuliucci, R. J.; Behnke, G.; Brown, R.; Shoup, D.; Riedel, T. M.; Plavchak, C.; Lininger, B. E.; Spehar, J. M. Moving towards fast characterization of polymorphic drugs by solid-state NMR spectroscopy. *J. Pharm. Biomed. Anal.* **2018**, *148*, 163−169.

(47) Tatton, A. S.; Pham, T. N.; Vogt, F. G.; Iuga, D.; Edwards, A. J.; Brown, S. P. Probing intermolecular interactions and nitrogen protonation in pharmaceuticals by novel ^{15}N-edited and 2D ^{14}N-^{1}H solid-state NMR. *CrystEngComm* **2012**, *14*, 2654−2659.

(48) Bauer-Brandl, A. Polymorphic transitions of cimetidine during manufacture of solid dosage forms. *Int. J. Pharm.* **1996**, *140*, 195−206.

(49) Guzmán-Afonso, C.; Hong, Y.-l.; Colaux, H.; Iijima, H.; Saitow, A.; Fukumura, T.; Aoyama, Y.; Motoki, S.; Oikawa, T.; Yamazaki, T.; Yonekura, K.; Nishiyama, Y. Understanding hydrogen-bonding structures of molecular crystals via electron and NMR nano-crystallography. *Nat. Commun.* **2019**, *10*, 3537.

(50) Bennett, A. E.; Rienstra, C. M.; Auger, M.; Lakshmi, K. V.; Griffin, R. G. Heteronuclear decoupling in rotating solids. *J. Chem. Phys.* **1995**, *103*, 6951−6958.

(51) Alderman, D. W.; McGeorge, G.; Hu, J. Z.; Pugmire, R. J.; Grant, D. M. A sensitive, high resolution magic angle turning experiment for measuring chemical shift tensor principal values. *Mol. Phys.* **1998**, *95*, 1113−1126.

(52) McGeorge, G.; Hu, J. Z.; Mayne, C. L.; Alderman, D. W.; Pugmire, R. J.; Grant, D. M. Technique for importing greater evolution resolution in multidimensional NMR spectrum. *J. Magn. Reson.* **1997**, *129*, 134−144.

(53) Clark, S. J.; Segall, M. D.; Pickard, C. J.; Hasnip, P. J.; Probert, M. J.; Refson, K.; Payne, M. C. First principles methods using CASTEP. *Z. Kristallogr. - Cryst. Mater.* **2005**, *220*, 567−570.

(54) Hammer, B.; Hansen, L. B.; Nørskov, J. K. Improved adsorption energetics within density-functional theory using revised Perdew-Burke-Ernzerhof functionals. *Phys. Rev. B: Condens. Matter Mater. Phys.* **1999**, *59*, 7413−7421.

(55) Yates, J. R.; Pickard, C. J.; Mauri, F. Calculation of NMR chemical shifts for extended systems using ultrasoft pseudopotentials. *Phys. Rev. B: Condens. Matter Mater. Phys.* **2007**, *76*, 024401.

(56) Yates, J. R.; Pickard, C. J.; Payne, M. C.; Mauri, F. Relativistic nuclear magnetic resonance chemical shifts of heavy nuclei with pseudopotentials and the zeroth-order regular approximation. *J. Chem. Phys.* **2003**, *118*, 5746−5753.

(57) Monkhorst, H. J.; Pack, J. D. Special points for Brillouin-zone integrations. *Phys. Rev. B* **1976**, *13*, 5188−5192.

(58) Pfrommer, B. G.; Côté, M.; Louie, S. G.; Cohen, M. L. Relaxation of crystals with the quasi-Newton method. *J. Comput. Phys.* **1997**, *131*, 233−240.

(59) McNellis, E. R.; Meyer, J.; Reuter, K. Azobenzene at coinage metal surfaces: role of dispersive van der Waals interactions. *Phys. Rev. B: Condens. Matter Mater. Phys.* **2009**, *80*, 205414.

(60) Pickard, C. J.; Mauri, F. All-electron magnetic response with pseudopotentials: NMR chemical shifts. *Phys. Rev. B: Condens. Matter Mater. Phys.* **2001**, *63*, 245101.

(61) Schreckenbach, G.; Ziegler, T. Calculation of NMR shielding tensors using gauge-including atomic orbitals and modern density functional theory. *J. Phys. Chem.* **1995**, *99*, 606−611.

(62) Adamo, C.; Barone, V. Toward reliable density functional methods without adjustable parameters: the PBE0 model. *J. Chem. Phys.* **1999**, *110*, 6158−6170.

(63) Krykunov, M.; Ziegler, T.; Lenthe, E. v. Hybrid density functional calculations of nuclear magnetic shieldings using Slater-type orbitals and the zeroth-order regular approximation. *Int. J. Quantum Chem.* **2009**, *109*, 1676−1683.

(64) Alderman, D. W.; Sherwood, M. H.; Grant, D. M. Comparing, modeling, and assigning chemical-shift tensors in the cartesian, irreducible spherical, and icosahedral representations. *J. Magn. Reson., Ser. A* **1993**, *101*, 188−197.

(65) Soss, S. E.; Flynn, P. F.; Iuliucci, R. J.; Young, R. P.; Mueller, L. J.; Hartman, J.; Beran, G. J. O.; Harper, J. K. Measuring and modeling highly accurate ^{15}N chemical shift tensors in a peptide. *ChemPhysChem* **2017**, *18*, 2225−2232.

(66) Harris, R. K.; Olivieri, A. C. Quadrupolar effects transferred to spin-1/2 magic-angle spinning spectra of solids. *Prog. Nucl. Magn. Reson. Spectrosc.* **1992**, *24*, 435−456.

(67) Strohmeier, M.; Alderman, D. W.; Grant, D. M. Obtaining molecular and structural information from ^{13}C−^{14}N systems with ^{13}C FIREMAT experiments. *J. Magn. Reson.* **2002**, *155*, 263−277.

(68) Strohmeier, M.; Stueber, D.; Grant, D. M. Accurate ^{13}C and ^{15}N chemical shift and ^{14}N quadrupolar coupling constant calculations in

amino acid crystals: zwitterionic, hydrogen-bonded systems. *J. Phys. Chem. A* **2003**, *107*, 7629−7642.
(69) Johnston, J. C.; Iuliucci, R. J.; Facelli, J. C.; Fitzgerald, G.; Mueller, K. T. Intermolecular shielding contributions studied by modeling the ^{13}C chemical-shift tensors of organic single crystals with plane waves. *J. Chem. Phys.* **2009**, *131*, 144503.
(70) Liu, F.; Phung, C. G.; Alderman, D. W.; Grant, D. M. Carbon-13 chemical shift tensors in methyl glycosides, comparing diffraction and optimized structures with single-crystal NMR. *J. Am. Chem. Soc.* **1996**, *118*, 10629−10634.
(71) Laskowski, R.; Blaha, P.; Tran, F. Assessment of DFT functionals with NMR chemical shifts. *Phys. Rev. B: Condens. Matter Mater. Phys.* **2013**, *87*, 195130.
(72) Laskowski, R.; Blaha, P. Understanding of ^{33}S NMR shielding in inorganic sulfides and sulfates. *J. Phys. Chem. C* **2015**, *119*, 731−740.

https://dx.doi.org/10.1021/acs.jpca.0c00421
J. Phys. Chem. A 2020, 124, 3109−3119